PAPER

Check for updates

DFT calculations and giant dielectric responses in $(Ni_{1/3}Nb_{2/3})_xTi_{1-x}O_2$†

Nateeporn Thongyong, Prasit Thongbai [ID] and Pornjuk Srepusharawoot [ID] *

The origins of dielectric responses in Ni^{2+} and Nb^{5+} co-doped TiO_2 were explored considering intrinsic and extrinsic effects. DFT calculations demonstrated that Ni^{2+} doping induced oxygen vacancies, while Nb^{5+} doping generated free electrons. Theoretical predictions indicated complex defect dipoles forming in the rutile structure, contributing to overall dielectric responses. Theoretical calculations also showed a possible linear alignment of $Ni^{2+}-2Nb^{5+}$ without oxygen vacancies, especially in high doping concentrations. Experimentally, $(Ni_{1/3}Nb_{2/3})_xTi_{1-x}O_2$ ceramics (x = 1%, 2.5%, and 10%) were synthesized. The substantial dielectric response at room temperature, attributed to factors like defect dipoles and grain boundary/surface barrier layer capacitor (GBLC/SBLC) effects, increased with higher doping levels. However, in a temperature range where GBLC/SBLC effects were suppressed, the dielectric response decreased with increased doping, likely due to self-charge compensation between $Ni^{2+}-2N^{b5+}$. Notably, $(Ni_{1/3}Nb_{2/3})_xTi_{1-x}O_2$ with x = 2.5% exhibited a high dielectric permittivity of 10^4 and a low loss tangent of 0.029 at 1 kHz. Moreover, the dielectric permittivity changed by less than $\pm15\%$ (compared to 25 °C) at 150 °C. This work provides an understanding of the origins of dielectric responses in co-doped TiO_2 and optimizes the doping concentration to achieve the best dielectric performance.

1 Introduction

Titanium dioxide (TiO_2) and its derivatives have garnered significant attention in the realm of materials science and engineering due to their exceptional dielectric properties and diverse applications.[1–3] In the constant pursuit of high performance, high reliability, and low electric power consumption in energy storage and miniaturized devices, there is a growing focus on materials with 'high' or 'giant' dielectric permittivity.[1,4–6] High-quality dielectric materials present an opportunity to develop high-performance capacitor applications.[7,8] According to the Electronics Industries Alliance (EIA), class II ceramic capacitors (such as X7R, X8R, and X9R capacitors) are recognized as high-performance capacitors and continue to be in development.[7,9] These capacitors demand minimal variation in capacitance with temperature, not exceeding $\pm15\%$ within a specific range. This requirement presents a significant challenge to overcome.

In 2013, Hu *et al.*[1] reported the excellent dielectric properties of (In^{3+}, Nb^{5+}) co-doped TiO_2 ceramics (INTO). The remarkable dielectric permittivity (ε') of approximately 6×10^4 and low loss tangent (tan δ) of less than 0.02 across a wide frequency and

temperature range were achieved. Subsequently, a series of acceptor/donor co-doped TiO_2 materials were widely investigated, involving trivalent acceptors and other acceptors. For instance, acceptor dopants (A^+, B^{2+}, C^{3+}), isovalent dopant (I^{4+}), and donor dopants (D^{5+}) (A = Ag or Li,[10,11] B = Mg, Zn, Sr, Cu or Ca,[12–15] C = Al, Sm, Bi, Fe, In, Dy, Ga, Gd, Yb, or Sc,[16–20] I = Zr,[21] and D = Nb^{5+}, Sb^{5+}, and Ta^{5+} (ref. 1 and 22–26)).

In addition to the exploration of high dielectric performance materials, it is crucial to comprehend the underlying origin of their dielectric properties. The electron-pinned defect dipole (EPDD) mechanism represents a novel approach for elucidating the exceptional dielectric response within co-doped TiO_2 systems.[1,26,27] Taking into account the substitution of the donor Nb^{5+} ions for the Ti^{4+} sites, free electrons are generated, resulting in an increase in ε' and tan δ. In order to suppress a large tan δ value, the introduction of oxygen vacancies was employed through acceptor doping, particularly with In^{3+}. Doping acceptors or donors onto the Ti^{4+} sites leads to the formation of internal defect clusters, such as $2In^{3+} - V_o^{\cdot\cdot} + 2Ti^{3+}(2e + 2Ti^{4+}) + 2Nb^{5+} + Ti^{4+}$.[1] The dielectric properties of various acceptor/donor co-doped TiO_2 systems have been elucidated through the EPDD concept.[1,23,28,29] The sole EPDD mechanism still lacks a clear explanation for the overall dielectric properties over a wide frequency–temperature range. Additionally, the internal barrier layer capacitor (IBLC), electron hopping, and surface barrier layer capacitor (SBLC) models are widely employed to elucidate the contribution to the dielectric response.[16,17,22,30–33] Based on previous literature, the

Giant Dielectric and Computational Design Research Group (GD–CDR), Institute of Nanomaterials Research and Innovation for Energy (IN–RIE), Department of Physics, Faculty of Science, Khon Kaen University, Khon Kaen 40002, Thailand. E-mail: spornj@kku.ac.th

majority of mechanisms is described in relation to trivalent acceptors. Surprisingly, few studies have explored the dielectric response in the context of bivalent acceptors, even though they also offer remarkable dielectric properties. For instance, (Mg^{2+}, Ta^{5+}),[29] (Mg^{2+}, Nb^{5+}),[34] and (Zn^{2+}, Nb^{5+})[23] co-doped TiO_2 systems exhibit excellent dielectric characteristics. Thus, in this research work, Ni^{2+} ions have been chosen as acceptors due to their appropriate ionic radius of approximately 69 pm.[35] The suitable ionic radius can readily facilitate the formation of EPDDs or remarkable defect dipoles.[23,29,34] Unfortunately, the dielectric properties of (Ni^{2+}, Nb^{5+}) co-doped TiO_2 have not been reported before.

Defects and their associated dipoles have emerged as crucial factors influencing the dielectric behavior of these materials. Defects, such as vacancies, interstitials, and substitutions, can significantly alter the local electronic structure and charge distribution, thereby inducing dipole moments within the crystal lattice.[36] Understanding the impact of these defect-induced dipoles on the dielectric response is paramount for tailoring and optimizing the performance of TiO_2-based materials in various technological applications.[1,3,36] Density Functional Theory (DFT) has proven to be an indispensable computational tool for investigating the electronic and structural properties of materials at the atomic scale. This approach enables a comprehensive exploration of the underlying mechanisms governing the macroscopic dielectric response observed in TiO_2-based materials. Therefore, this study also aims to delve into the realm of defect dipoles and their profound influence on the giant dielectric response exhibited by TiO_2-based materials. Furthermore, the experimental data were also designed to support together between the theoretical and experimental results.

In this study, we conducted DFT calculations to predict the potential formation of defect dipoles. Ceramics of ($Ni_{1/3}Nb_{2/3}$)$_x$$Ti_{1-x}O_2$ (with $x = 1\%$, 2.5%, and 10%) were prepared. A high ε' with low $\tan\delta$ was achieved at a 2.5% co-doping concentration. The temperature-dependent dielectric properties were investigated over a range of 20 to 483 K. Four relaxations were observed, signifying mechanisms within the dielectric properties. These relaxations provide insights into explaining the origins of the exceptional dielectric properties. Additionally, the contribution of dielectric values to each relaxation was determined to ascertain the most influential mechanisms on dielectric properties. Furthermore, fundamental characteristics were examined, including X-ray diffraction (XRD), Scanning Electron Microscopy (SEM), Raman spectroscopy, and X-ray photoelectron spectroscopy (XPS).

2   Experimental details

All the starting raw materials were obtained from Sigma-Aldrich, which include TiO_2 (99.9% purity), NiO (99.99% purity), and Nb_2O_5 (Sigma-Aldrich, 99.99% purity). The conventional solid-state method formed the powder. Details were provided in the previous published works.[24] The powders are neatly ground before being pressed into a disc shape by uniaxial compression at ~180 MPa. After that, sintered at 1350 °

C for 2 h, with a heating rate of 3 °C min^{-1} in a normal atmosphere, was used to obtain the ($Ni_{1/3}Nb_{2/3}$)$_x$$Ti_{1-x}O_2$ ($x = 1\%$, 2.5% and 10%) ceramics and name as 1%NiNTO, 2.5%NiNTO and 10%NiNTO (xNiNTO).

The phase structure of these co-doped ceramics was initially assessed using XRD technique (PANalytical, EMPYREAN). Subsequently, the microstructure of the co-doped ceramics was examined using SEM (SEC, SNE-4500M). For elemental distribution analysis, SEM-mapping was conducted using a focused ion beam-field emission scanning electron microscopy (FEI, QUANTA 450) equipped with energy-dispersive X-ray spectroscopy (EDS). Details of Raman spectroscopy, XPS, and the dielectric measurements were provided in the previous work.[24] Before measuring the dielectric properties, we applied silver paste to both sides of the sample and then heated it at 600 °C for 0.5 h. The dielectric response was assessed using a KEYSIGHT E4990A Impedance Analyzer, applying an AC oscillation voltage of 0.5 V. Measurements were conducted over frequency and temperature ranges of 40 to 10^6 Hz and −258 to 210 °C, respectively.

For computational details, in our works, the Vienna *ab initio* simulation package (VASP),[37] which is a code based on the density functional theory has been used. Additionally, spin-polarized calculations were used. The projector augmented wave approach and the Perdew–Burke–Ernzerhof functional exchange–correlation functional were employed. The energy cutoff and k-point mesh of reciprocal space are 600 eV and $5 \times 3 \times 3$, respectively. For TiO_2 structure, rutile phase has been used. Moreover, in these calculations, the $2 \times 3 \times 5$ supercell of this phase was carried out. The chemical formula for this supercell is $Ti_{60}O_{120}$.

3   Results and discussion

Fig. 1 represents the two possible positions of the oxygen vacancy (V_o) in the Ni doped TiO_2 structure. Our calculation results disclosed that total energy when the V_o is at position A is lower than that when the V_o is located at positon B for 0.29 eV. Hence, the V_o is preferably close to the Ni ion. Based on this observation, the oxygen vacancy can be induced by the Ni in this structure. By using the structure with the V_o is at position A as an initial structure, two Nb atoms are inserted into this structure.

The total energy of two Nb atoms in the TiO_2 with NiV_o inside was calculated, as displayed in Fig. 2(a). Four different positions of Nb in the Ni doped TiO_2 host are displayed by structures I–IV in Fig. 2(b). According to structure I, two Nb atoms are rather far from both Ni and V_o. For structure II, Nb atoms approach the V_o side. Structure III represents the Nb atoms located at the Ni side. Lastly, two Nb atoms form as the Nb_2Ni chain presented by structure IV. The total energy of these four structures is also presented in Fig. 2. We found that total energy of the structure II was the lowest followed by III, I and IV, respectively. Consequently, structure II was a stable structure. In other words, two Nb ions prefer to be close to the V_o.

We also investigated the most stable structure of the Ni and Nb co-doped TiO_2 without the V_o inside the structure. The total
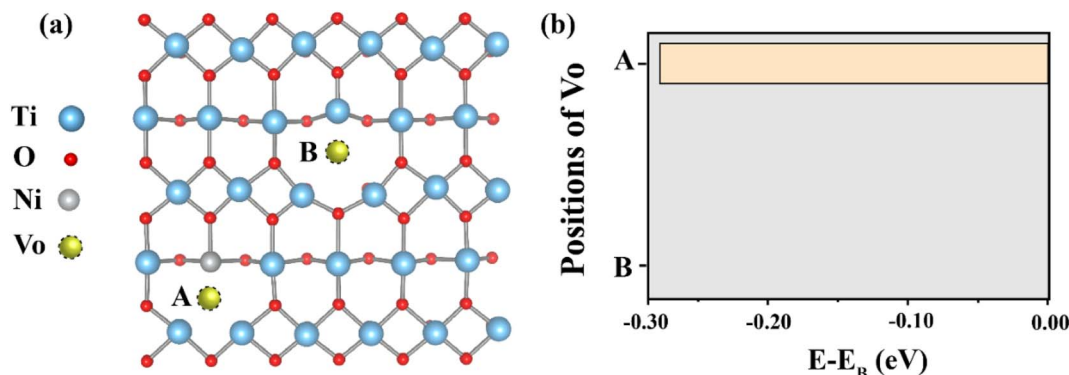
Fig. 1 (a) Two possible positions of the oxygen vacancy in the Ni doped TiO_2 structure. For position A, the oxygen vacancy is near the Ni, whereas this vacancy does not interact with the Ni when it is located at position B. (b) Total energy corresponds to two positions of the oxygen vacancy.
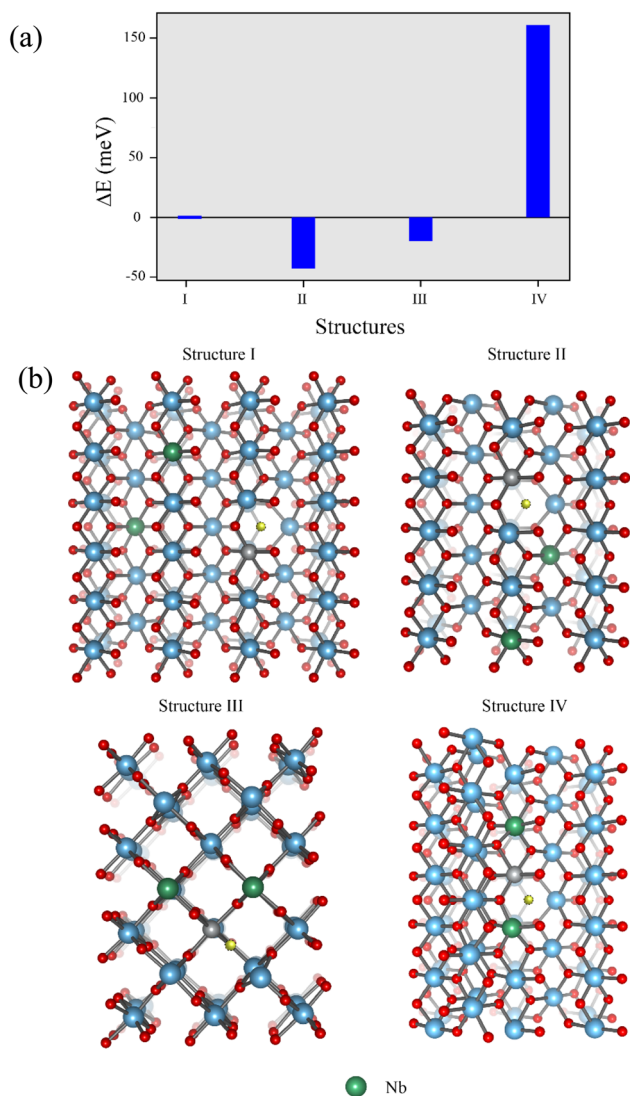

Fig. 2 (a) Total energy of two Nb atoms in the TiO_2 with NiV_O inside. (b) Four different positions of Nb in the Ni doped TiO_2: structure I, two Nb atoms are isolated from both Ni and V_O. Structures II and III, two Nb atoms approach the V_O and Ni sides, respectively. Structure IV, Ni and two Nb atoms form as a Nb_2Ni chain.

energy for the two distinct configurations of Nb_2Ni is illustrated in Fig. 3(a). As shown in Fig. 3(b), for Nb_2Ni chain, two Ni atoms are enclosed by two Nb atoms. According to the Nb_2Ni triangular structure, as shown in Fig. 3(c), Ni and Nb atoms are located at the corner of the triangle. Total energy corresponding to these structures is presented in Fig. 3(a). Nb_2Ni chain is more stable than the Nb_2Ni triangle due to lowering in total energy. Hence, based on our calculations, the most stable structure of the Ni and Nb co-doped TiO_2 without the Vo is the Nb_2Ni chain. In this scenario, there is no requirement for any charge compensations, such as V_O or free electrons.

The XRD patterns of the xNiNTO samples at various concentrations are presented in Fig. 4. All xNiNTO ceramics exhibited a tetragonal unit cell structure with the $P4_2/mnm$ space group. The primary diffraction peak corresponds to the pure rutile TiO_2 crystal structure (JCPDS #21-1276).[38,39] No secondary phases are detected, which can be attributed to the close ionic radii of Ni^{2+} ($\sim$69 pm) and Nb^{5+} ($\sim$64 pm) to that of Ti^{4+} ($\sim$60.5 pm), in accordance with the Hume-Rothery rules.[18] The lattice parameters of the samples were determined through Rietveld refinement and are detailed in Table 1. The a and c values increase with higher co-doping content. This outcome aligns with observations in other acceptor/donor co-doped TiO_2 materials.[1,40,41] The substitution of co-dopant Ni^{2+} and Nb^{5+} ions at the Ti^{4+} sites leads to a significant expansion of the lattice parameters. This expansion provides crucial evidence supporting the incorporation of Ni^{2+} and Nb^{5+} ions at the Ti^{4+} sites without the emergence of secondary phases.[35] This expansion can be attributed to the larger ionic radii of the dopants compared to Ti^{4+}. It is important to note that the Ti^{3+}, Ti^{4+}, $V_O^{\cdot\cdot}$, Ni^{2+}, and Nb^{5+} were confirmed to exist in the samples using XPS technique, as shown in Fig. S1 and S2 (ESI†).

To provide further confirmation of the substitution co-doping within the Ti^{4+} sites, Raman spectroscopy was employed (Fig. 5). Four distinct Raman characteristics (B_{2g}, B_{1g}, E_g, and A_{1g}) are consistent with the rutile TiO_2 phase.[42] Specifically, the B_{1g} mode corresponds to the O–Ti–O bending vibration, the E_g mode involves oxygen atoms moving out of the crystal lattice along the c-axis, and the A_{1g} mode signifies O–Ti–O stretching vibration.[22,42] Generally, the observed shifts in the
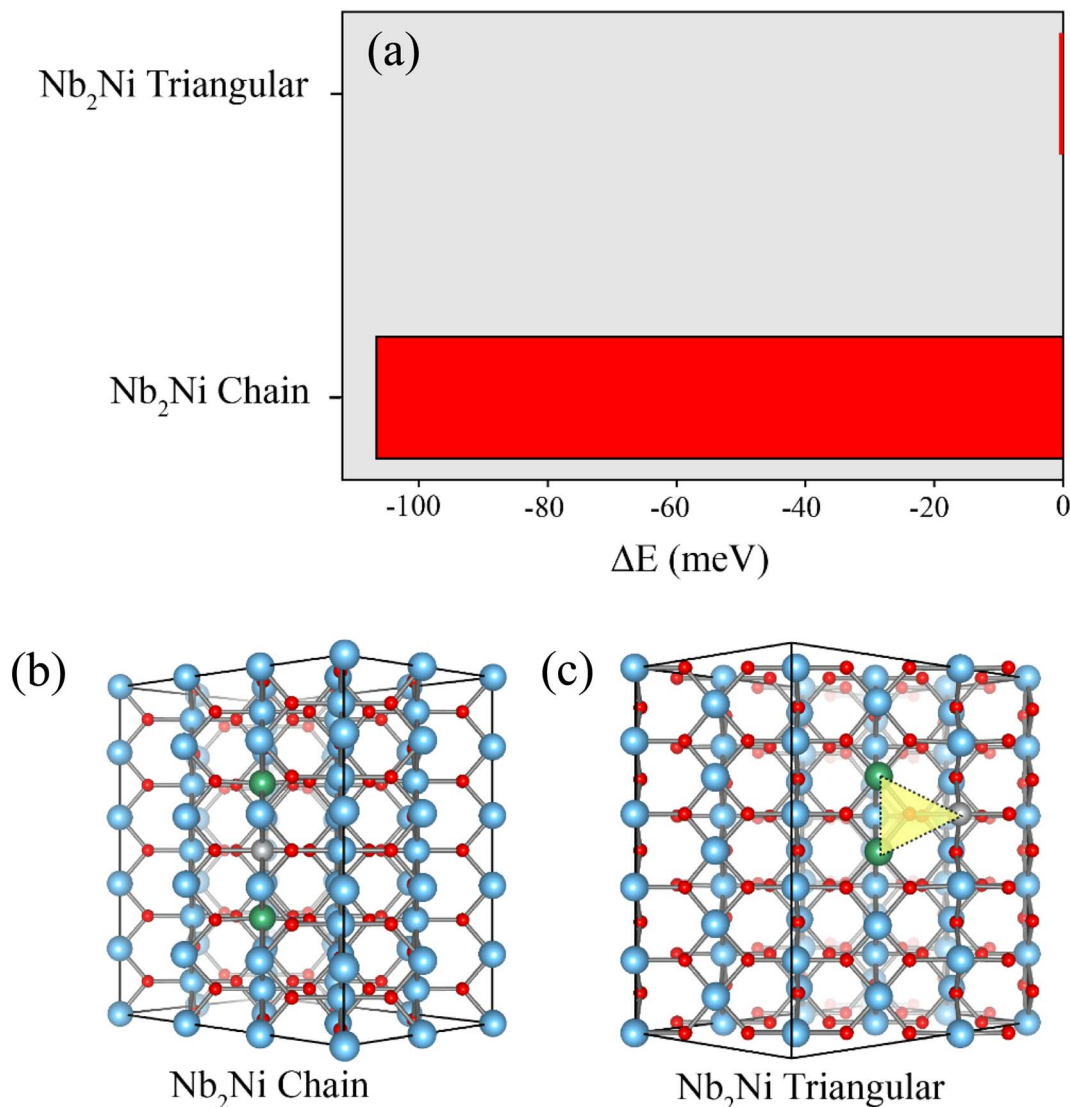
Fig. 3 (a) Total energy associated with Nb_2Ni in two distinct configurations. (b) Chain configuration of Nb_2Ni. (c) Triangular configuration of Nb_2Ni.

Raman peaks of rutile TiO_2 with varying co-doping concentration suggest changes in the crystal environment due to the incorporation of foreign ions. As depicted in Table 1, the A_{1g} peak demonstrates a shift towards higher wavelengths, signifying the impact of substituted dopants on the O–Ti–O stretching vibration. This shift is attributed to the distinct ionic radii between the dopants and host ions. The E_g peaks of all xNiNTO ceramics exhibit a shift to lower wavelengths with increasing co-doping concentration. This result indicated an increase in V_o concentration.[42] The introduction of Ni^{2+} into the Ti^{4+} site necessitates a positive charge for charge equilibrium, leading to the generation of V_o according to the equation:

$$NiO \xrightarrow{TiO_2} Ni''_{Ti} + V_o^{\cdot\cdot} + O_o \quad (1)$$
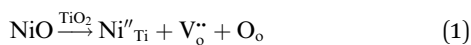
SEM micrographs of the xNiNTO sample are illustrated in Fig. 6(a)–(d). All ceramic specimens exhibited a morphology characterized by smooth-surfaced grains. The average grain sizes for the 1%NiNTO, 2.5%NiNTO, and 10%NiNTO samples are measured and found to be 10.5 ± 4.2, 9.8 ± 4.9, and 4.9 ± 2.3 μm, respectively. As the co-doping $(Ni_{1/3}Nb_{2/3})_x$ increased from 1% to 2.5%, there was a slight change in grain size. However, a notable reduction in grain size was observed when the co-doping concentration rose from 2.5% to 10%. This suggests that Ni^{2+} and Nb^{5+} presence hindered grain growth within the samples.[43,44] According to previous work,[24,45] the mean grain sizes of TiO_2 were significantly reduced by factors of 2 and 3 when doped with 1.67 at% Ni^{2+} and 1 at% Nb^{5+}, respectively. Therefore, the reduction in grain size of the xNiNTO can be attributed to the substitution by both Ni^{2+} and Nb^{5+} dopants. For $BaTiO_3$ and $CaCu_3Ti_4O_{12}$ doped with high concentrations of Nb^{5+} or Ta^{5+},[46,47] significant grain growth inhibition was observed. This has been ascribed to the generation of space charges at grain boundaries. During the sintering
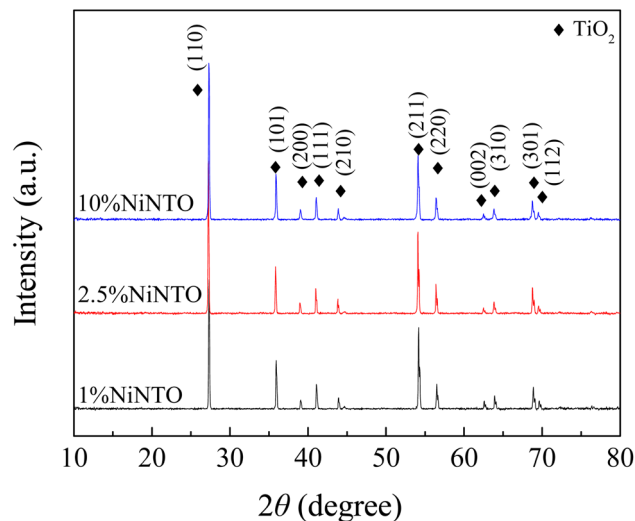
Fig. 4 XRD patterns of xNiNTO with various dopant concentrations.

Table 1 Lattice parameters (a and c), Raman shift, and density of TiO$_2$, 1%NiNTO, 2.5%NiNTO, and 10%NiNTO

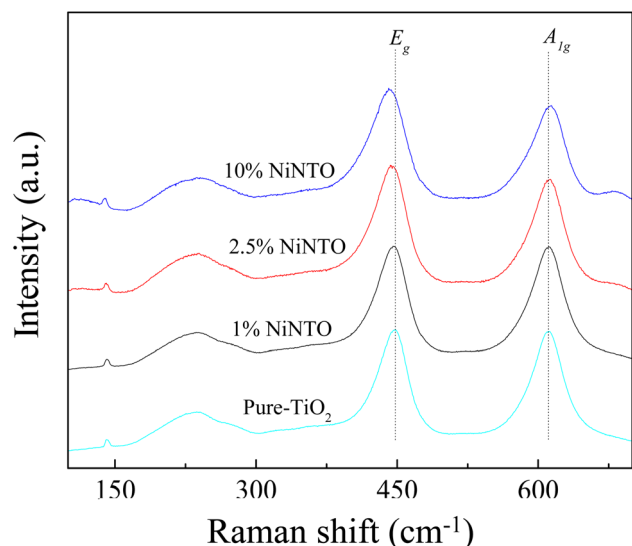| | Lattice parameters (Å) | | Raman shift (cm^{-1}) | | |
| | a | c | E$_g$ | A$_{1g}$ | Density (g cm^{-3}) |
Sample					
TiO$_2$	4.593(1)	2.959(3)	448.3	610.6	4.23
1%NiNTO	4.592(7)	2.960(8)	445.9	611.2	4.20
2.5%NiNTO	4.593(2)	2.960(9)	444.1	613.0	4.26
10%NiNTO	4.601(9)	2.966(5)	441.0	614.2	4.35

Fig. 5 Raman spectra of TiO$_2$ and xNiNTO with various dopant concentrations.

process, the diffusion rate of O^{2-} across grain boundaries, which contributes to grain growth, is impeded by space charges from accumulated free electrons (e$^-$). This is due to the repulsive force between O^{2-} and e$^-$.

Furthermore, the element on the surface was investigated using the FE-SEM mapping technique, as shown in Fig. 7. The results reveal the elemental distribution of Ti, O, Nb, and Ni on the surface of the 2.5%NiNTO sample. The highest concentration is observed for Ti and O elements, while Ni and Nb exhibit slightly lower contributions, likely attributed to their dopant contents.

The frequency-dependent behavior of ε' and tan δ for the xNiNTO samples is illustrated in Fig. 8(a) and (b), measured at room temperature. The ε' values for all the samples exhibit a slight dependence on frequency, while the tan δ values show notable sensitivity to frequency variations. Notably, the ε' value at approximately 30 °C for xNiNTO samples increases with higher co-dopant content. The increase in ε' with higher co-dopant content is consistent with the behavior observed in similar systems,[1] suggesting that the incorporation of Ni^{2+} and Nb^{5+} ions can enhance the dielectric response. The ε' and tan δ values at around 30 °C and 1 kHz for the xNiNTO ceramics are summarized in Table 2. Particularly high ε' values exceeding 10^4 were achieved at doping contents of x = 2.5% and 10%. Remarkably, the 2.5%NiNTO composition exhibited promising dielectric properties with an ε' of approximately 11 166 and a tan δ of 0.029 at 1 kHz. Interestingly, at 40 Hz, tan δ was as low as 0.01. This clearly demonstrates that the co-doping of Ni^{2+} and Nb^{5+} significantly influences the dielectric properties, potentially due to a range of contributing factors. Additionally, the co-doping content plays a crucial role, evident in the optimal co-doping content of 2.5%. The relationship between co-doping content and dielectric behavior further emphasizes the importance of precise tuning for optimal performance. The comparison of the ε' and tan δ values at approximately 30 °C and 1 kHz for 2.5%NiNTO and previous works is depicted in Fig. 8(c).[12,15,23,24,45,48–50] The comparative results reveal that 2.5% NiNTO, with its high ε' and tan δ values, shows promise for applications in capacitors. It should be noted that while a high ε' can be achieved in 5%Nb^{5+}-doped TiO$_2$, the tan δ was significantly large, approximately 0.5.[49] On the other hand, 1.67% Ni^{2+}-doped TiO$_2$ offered a low tan δ, but its ε' is only around 10^3.[24]

Dielectric spectroscopy assessments were performed on both the 2.5%NiNTO and 10%NiNTO ceramic materials across a temperature spectrum of 20 to 483 K. It should be noted that the temperature dependence of ε' for the 1%NiNTO ceramic was not assessed due to its pronounced tan δ value at lower frequency ranges. These findings are delineated in Fig. 9(a) and (b). The 10%NiNTO variant manifested a heightened temperature sensitivity, evidenced by a considerable augmentation in the ε' value in response to increasing temperatures. In contrast, the 2.5%NiNTO ceramic demonstrated superior temperature stability, maintaining a relatively constant ε' value, a trait corroborated by data depicted in Fig. 9(b). Moreover, when comparing the temperature coefficients of ε' ($\Delta\varepsilon'/\varepsilon'_{30}$), the 2.5% NiNTO ceramic exhibits changes within ±15% of the $\Delta\varepsilon'/\varepsilon'_{30}$ over a temperature range from 243 to 453 K.

As shown in Table 2 and Fig. 9(b), among the three samples, the 2.5%NiNTO ceramic displayed both the lowest tan δ value and the most favorable temperature coefficient. Consequently,
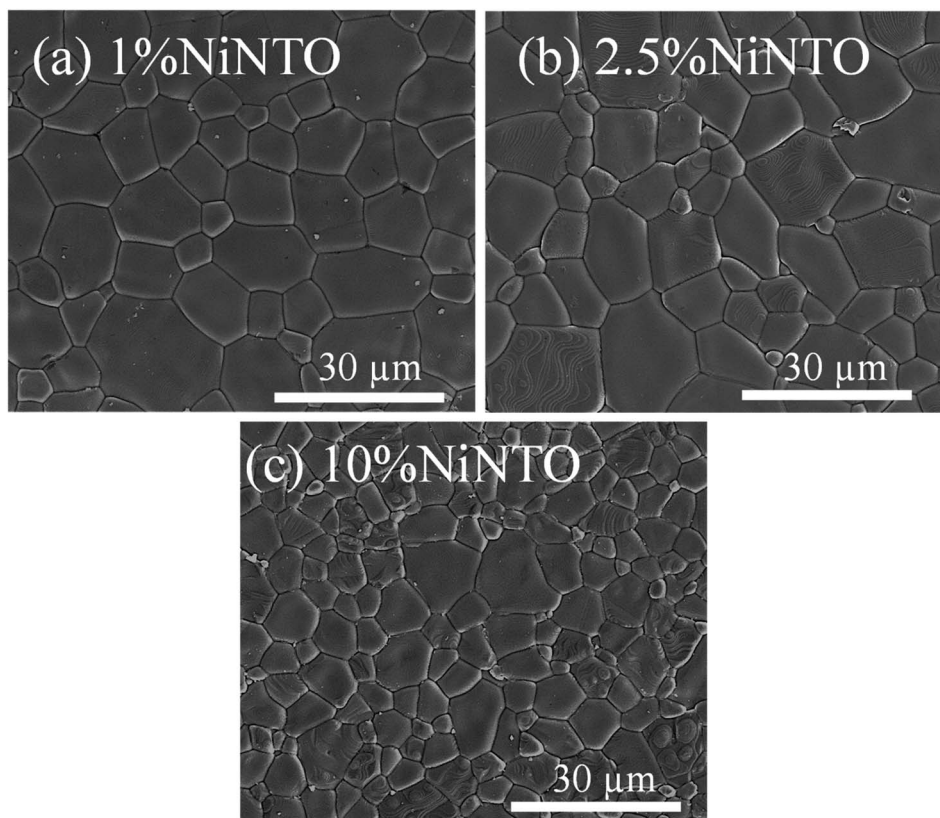
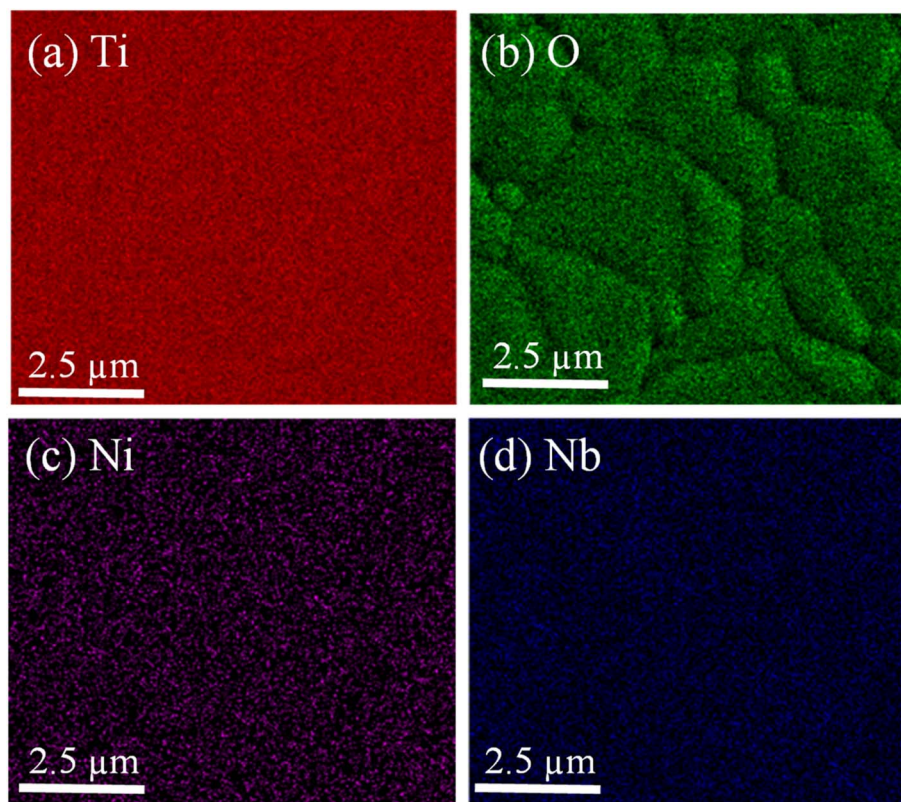**Fig. 6** SEM images of (a) 1%NiNTO, (b) 2.5%NiNTO, and (c) 10%NiNTO.

Fig. 7 SEM mapping images of 2.5%NiNTO for (a) Ti, (b) O, (c) Ni, and (d) Nb elements.
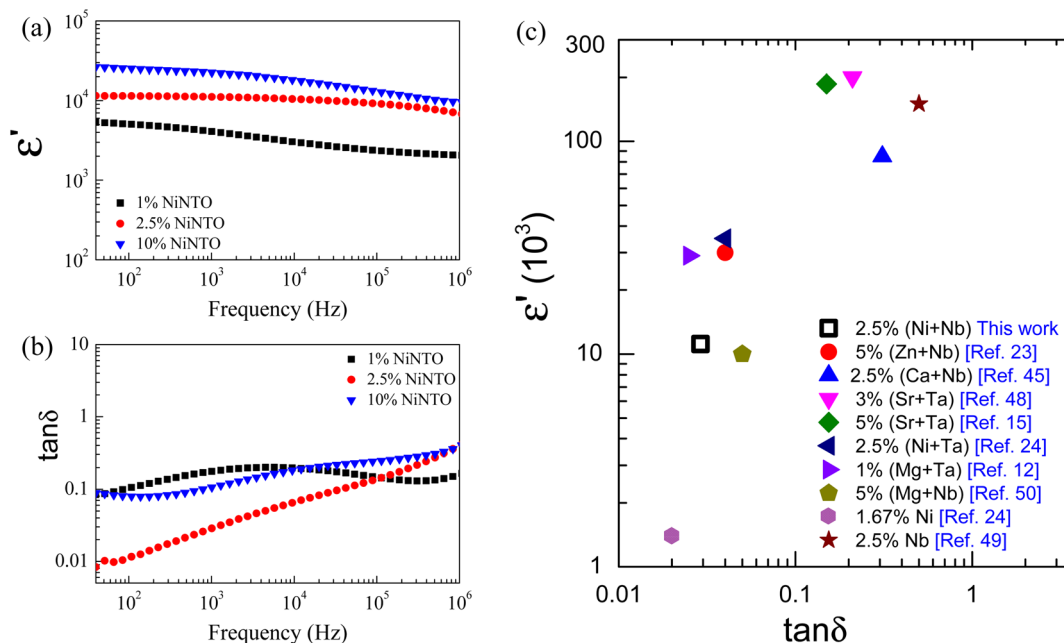
Fig. 8 Frequency dependence of dielectric properties of (a) ε' and (b) $\tan \delta$ at ~30 °C for 1%NiNTO, 2.5%NiNTO, and 10%NiNTO. (c) ε' and $\tan \delta$ at ~30 °C and 1 kHz of 2.5%NiNTO compared to previous works.

Table 2 Dielectric permittivity (ε'), loss tangent ($\tan \delta$) at 1 kHz, and relaxation activation energies of xNiTTO ceramics

Sample	Dielectric properties (~30 °C/1 kHz)		E_a (eV)		
	ε'	$\tan \delta$	R1	R2	R3
1%NiNTO	4090	0.177	—	—	—
2.5%NiNTO	11 166	0.029	0.037	0.103	0.527
10%NiNTO	22 502	0.106	0.058	0.129	0.304

we selected the 2.5% sample for detailed analysis, with the belief that its properties can be further fine-tuned to better suit capacitor applications. Fig. 10(a) and (b) depict the ε' and $\tan \delta$ as functions of temperature and frequency, respectively, showing multiple relaxation responses of the 2.5%NiNTO ceramic. Several dielectric relaxations in the 2.5%NiNTO ceramic were observed, labeled as R1, R2, R3, and R4 in ascending order from low to high temperatures. A step-like decrease in ε' was accompanied by a shift in the $\tan \delta$ peak position, which moved to higher frequencies as the temperature
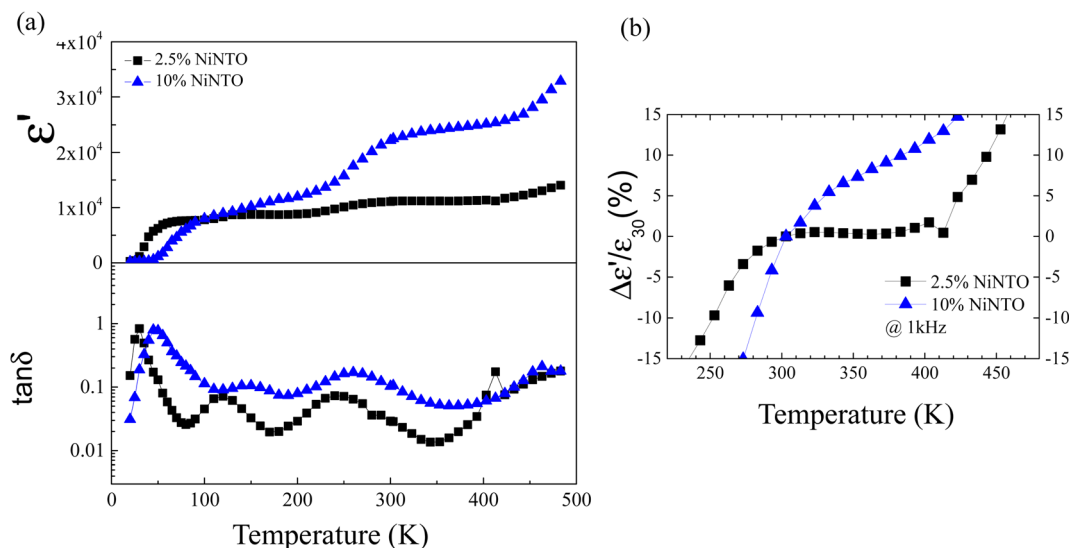

Fig. 9 (a) Temperature-dependent behaviors of ε' and $\tan \delta$ for ceramics composed of 2.5%NiNTO and 10%NiNTO, measured over a temperature range of 20 to 483 K. (b) Temperature coefficient of ε' at a frequency of 1 kHz for 2.5%NiNTO and 10%NiNTO.

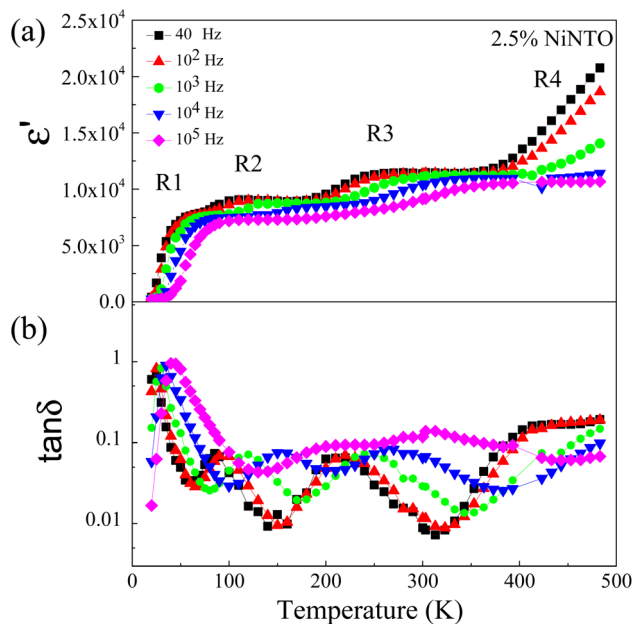© 2023 The Author(s). Published by the Royal Society of Chemistry

Fig. 10 Dielectric relaxation steps in 2.5%NiNTO contributed from different mechanisms of polarizations: (a) ε' and (b) $\tan \delta$ as functions of temperature and frequency.

increased. This observation signifies the thermally activated dielectric relaxation phenomenon. The R1, R2, and R3 relaxations were evident in the temperature ranges of 20–70 K, 100–180 K, and 190–260 K, respectively. The R4 relaxation emerged at temperatures exceeding 400 K. In xNiNTO ceramics, when we observe an ε' value around room temperature (∼300 K), it is important to note that there are at least four primary associated polarizations that collaborate to contribute to the dielectric response, resulting in such an ε' value at 300 K. First, a low ε' value of roughly 230 below 20 K can be attributed to electronic and ionic polarization. The contributions from R1, R2, and R3 will be discussed in subsequent sections. It should be noted that the contribution from R4 occurs at temperatures exceeding 400 K. Nevertheless, the R4 relaxation will also be described.

To better understand the physical mechanism underlying the dielectric relaxations, the imaginary part ($\varepsilon'' = \varepsilon' \tan \delta$) of complex dielectric permittivity ($\varepsilon^* = \varepsilon' - i\varepsilon''$) for 2.5%NiNTO as a function of frequency has been plotted in different temperature ranges, as shown in Fig. 11(a)–(c). Generally, the Debye model accounts for the dielectric relaxation using the Arrhenius equation as:

$$f = f_0 \exp\left(-\frac{E_a}{k_B T}\right), \tag{2}$$

where f is the frequency at the relaxation peak, f_0 is the pre-exponential factor, E_a represents the activation energy required for the relaxation process, T is the absolute temperature, and k_B is Boltzmann's constant. The relaxations across different temperature ranges at various frequencies can be identified from the peak values of ε''. The activation energy, E_a, can then be determined using the Arrhenius relation.

We focused on the contribution of the R1 relaxation to the dielectric response, which was approximately 7.5×10^3. Fig. 11(a) illustrates the frequency dependence of ε'' across temperatures ranging from 30 to 75 K, where a distinct ε'' peak is evident. As the temperature rises, the relaxation peak shifts towards higher frequencies, a characteristic of thermally activated relaxation. The E_a of 0.037 eV was calculated, as shown in Fig. 11(d). This E_a value, being modest, is less than the conduction activation energy within the semiconducting grains. According to the DFT calculations presented in Fig. 1–3, it was theoretically established that defect clusters associated with $V_o^{\cdot\cdot}$ and free electrons from Nb^{5+} were formed, leading to the creation of EPDDs conceptually. Consequently, the R1 relaxation is likely related to the activation or freezing of electrons in defect-dipole clusters. This interpretation aligns with the DFT calculations, which confirm the existence of EPPDs arising from acceptor and donor dopants.[51]

The R2 relaxation was then characterized. In this study, the formation of some Ti^{3+} occurred due to the doping of donor ions, while doping with Ni^{2+} led to the creation of oxygen vacancies. The point defects associated with Ni''_{Ti}, $Nb^{\cdot}_{Ti}$, Ti'_{Ti} and $V_o^{\cdot\cdot}$ were formed and interconnected, aligning with the configurations predicted by the DFT calculation. A detailed examination of the R2 relaxation is provided in Fig. 11(b). An Arrhenius plot of the relaxation was derived from the linearly fitted curve, as illustrated in Fig. 11(d). The E_a for the R2 relaxation was calculated to be 0.103 eV. This value closely matches the activation energy associated with the movement of free electrons within the semiconducting grains. The E_a value is consistent with findings in +3/+5 co-doped TiO_2 and the grain of CCTO.[4,52,53] In giant dielectric oxides possessing an IBLC structure, previous studies have demonstrated that the activation energy for dielectric relaxation and the conduction activation energy within semiconducting grains are nearly identical.[53,54] Therefore, the origin of the R2 relaxation is attributed to the IBLC effect. The relaxation polarization at the grain boundary, framed by neighboring semiconducting grains, can be accentuated. Additionally, the relaxation time ($\tau = 1/2\pi f_{max}$) of the dipole moment for R2 rotates more slowly than that of the R1 relaxation. This can be attributed to the fact that free electrons confined in defect dipoles are more readily moved by the electric force from an applied field ($F = qE$) than the electron hopping between Ti^{3+}–O^{2-}–Ti^{4+}. The movement of a negatively charged electron is often hindered by the negative charges of the O^{2-} ion. As a result, it takes longer for the electron to move and accumulate at the grain boundary, leading to the production of interfacial polarization. At any given temperature, polarization from the IBLC effect requires a longer duration, indicating a larger relaxation time for R2.

Fig. 11(c) illustrates the relaxation peak of ε'' occurring below 10^5 Hz, corresponding to the R3 relaxation. The activation energy for the R3 relaxation, depicted in Fig. 11(e), is 0.527 eV. This value is possibly attributable to the SBLC effect.[24,55] Interfacial polarization predominates at the boundary between the outer surface layer and the inner semiconducting core, leading to polarization relaxation.
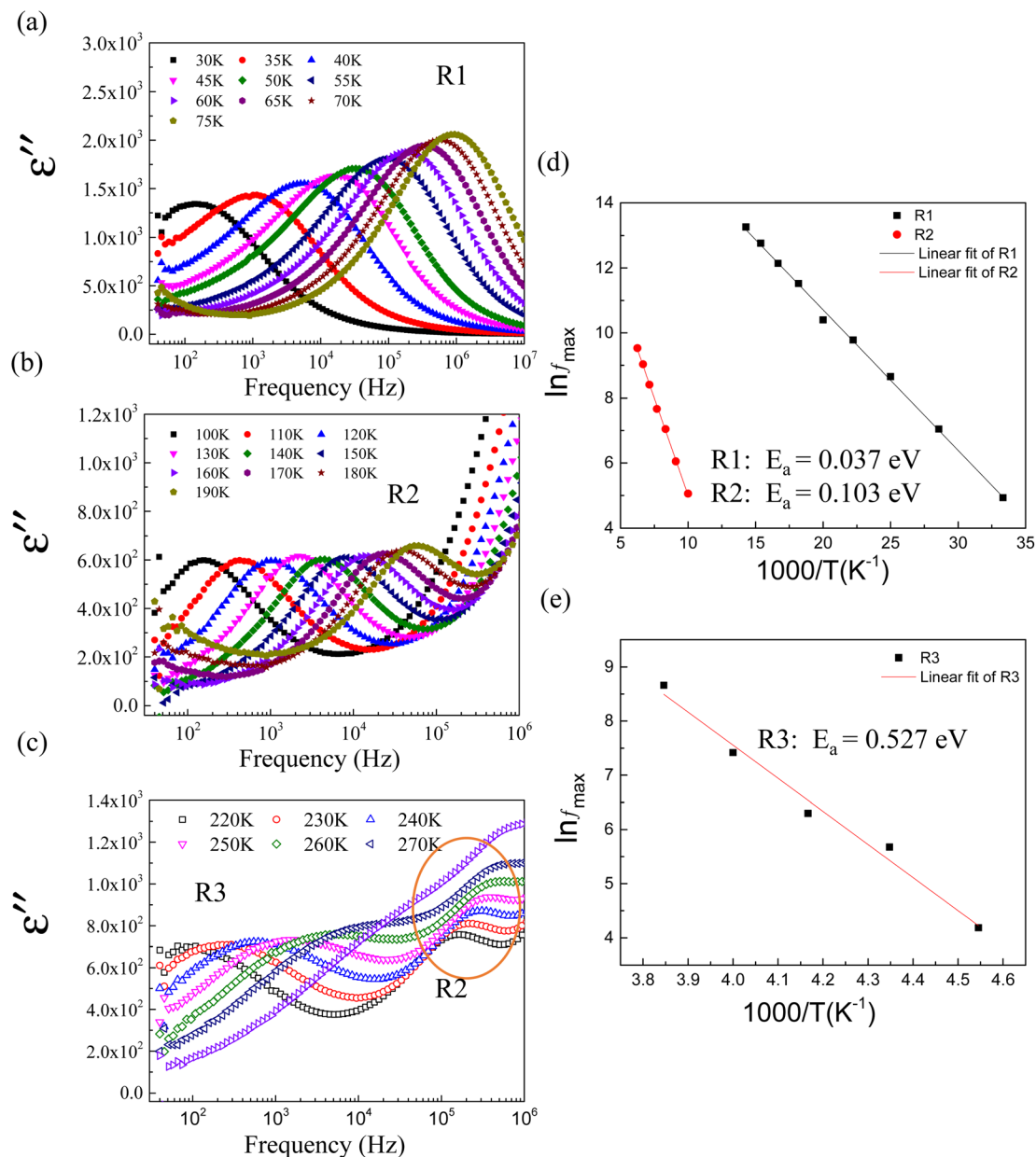
Fig. 11 Frequency dependence of ε'' ($\varepsilon'' = \varepsilon' \tan \delta$), expanding view of dielectric relaxations in 2.5%NiNTO: (a) R1, (b) R2, and (c) R3. (d) Arrhenius plot for R1 and R2 relaxations. (e) Arrhenius plot for R3 relaxation.

Additionally, results derived from the fitting of the Arrhenius equation for other co-doped TiO$_2$ contents are presented in Table 1. The mechanism underlying each relaxation remains consistent with that observed in 2.5%NiNTO. Notably, the R1 relaxation increases prominently from a concentration of 2.5% to 10%. These findings suggest that the relaxation of polarized electron confinement within the EPDD structure becomes more challenging to induce as co-doping content rises. This is evidenced by the R1 relaxation in the 10%NiNTO ceramic requiring greater activation energy than its 2.5%NiNTO counterpart.[56] This observation aligns with the DFT calculations, which forecast the formation of a linear alignment of Ni^{2+}–2Nb^{5+} without oxygen vacancies (self-charge compensation) as

co-doping content increases. Consequently, the EPDD concentration in the 10%NiNTO ceramic should be diminished compared to the 2.5%NiNTO ceramic. This is attributed to the self-charge compensation mechanism, which negates the formation of free electrons from Nb^{5+} doping ions.[1] The activation energy for the R2 relaxation escalates as co-doping concentration rises, indicating that the R2 relaxation demands more energy under increased co-doping. This can be linked to the anticipated self-charge compensation in the 10% NiNTO ceramic, leading to a reduced concentration of free electrons within the semiconducting grains and V$_\ddot{O}$. Thus, relaxation due to the IBLC effect in the 10%NiNTO ceramic, associated with semiconducting grains and insulating grain

boundaries, necessitates higher energy. Although the activation energy of the R3 relaxation pertains to the SBLC effect,[24] its trend diminishes in the 10%NiNTO ceramic. This suggests a reduced resistivity of the 10%NiNTO ceramic's insulating surface compared to the 2.5%NiNTO. This could be because the active acceptor ions in the 10%NiNTO were mitigated due to the self-charge compensation of Ni^{2+}–$2Nb^{5+}$. This results in a diminished Schottky barrier height at the interface between the semiconducting inner core and the outer layer.[57] Thus, less activation energy is needed for a dielectric response at this Schottky contact. Minimal energy is adequate to surpass a low Schottky barrier height. At elevated temperatures, the movement of $V_O^{\cdot\cdot}$ or oxygen ions becomes feasible, contributing to the dielectric response. Therefore, the R4 relaxation is associated with the DC conduction of $V_O^{\cdot\cdot}$ or O^{2-} ions.[5] This research has unveiled critical insights into dielectric relaxation, underscoring the intricate behaviors and mechanisms within co-doped TiO_2 ceramics. The profound interplay between material concentrations and their associated polarizations is pivotal, shaping the broader understanding of materials science.

4 Conclusion

The dielectric responses in Ni^{2+} and Nb^{5+} co-doped TiO_2 were comprehensively explored, considering both intrinsic and extrinsic effects. DFT calculations revealed that Ni^{2+} doping induced oxygen vacancies, while Nb^{5+} doping led to the generation of free electrons. Complex defect dipoles were predicted to form in the rutile structure, influencing the overall dielectric response. The theoretical findings also unveiled the potential for linear Ni^{2+}–$2Nb^{5+}$ alignment without oxygen vacancies at high doping concentrations. Experimentally, $(Ni_{1/3}Nb_{2/3})_xTi_{1-x}O_2$ ceramics ($x = 1\%$, 2.5%, and 10%) exhibited enhanced dielectric responses, attributed to defect dipoles and GBLC/SBLC effects. Notably, $(Ni_{1/3}Nb_{2/3})_xTi_{1-x}O_2$ with $x = 2.5\%$ demonstrated a high ε' of 10^4 and low $\tan\delta \sim 0.029$, while maintaining stability over a broad temperature range to 423 K (150 °C). This material showed the significant potential of tailored Ni^{2+}–Nb^{5+} co-doping strategies in enhancing dielectric properties.

Conflicts of interest

The authors declare no competing financial interests.

Acknowledgements

References

1. W. Hu, Y. Liu, R. L. Withers, T. J. Frankcombe, L. Norén, A. Snashall, M. Kitchin, P. Smith, B. Gong, H. Chen, J. Schiemer, F. Brink and J. Wong-Leung, *Nat. Mater.*, 2013, **12**, 821–826.
2. X. Chen, *Chin. J. Catal.*, 2009, **30**, 839–851.
3. X. Chen and S. S. Mao, *Chem. Rev.*, 2007, **107**, 2891–2959.
4. C. C. Homes, T. Vogt, S. M. Shapiro, S. Wakimoto and A. P. Ramirez, *Science*, 2001, **293**, 673–676.
5. J. Wu, C.-W. Nan, Y. Lin and Y. Deng, *Phys. Rev. Lett.*, 2002, **89**, 217601.
6. S. Krohns, P. Lunkenheimer, S. Meissner, A. Reller, B. Gleich, A. Rathgeber, T. Gaugler, H. U. Buhl, D. C. Sinclair and A. Loidl, *Nat. Mater.*, 2011, **10**, 899–901.
7. M. J. Pan and C. A. Randall, *IEEE Electr. Insul. Mag.*, 2010, **26**, 44–50.
8. Y. Wang, W. Jie, C. Yang, X. Wei and J. Hao, *Adv. Funct. Mater.*, 2019, **29**, 1808118.
9. A. J. Moulson and J. M. Herbert, *Electroceramics: materials, properties, applications*, Wiley, West Sussex, New York, 2nd edn, 2003.
10. P. Liang, J. Zhu, D. Wu, H. Peng, X. Chao and Z. Yang, *J. Am. Ceram. Soc.*, 2021, **104**, 2702–2710.
11. W. Li, Z. Liu, F. Zhang, Q. Sun, Y. Liu and Y. Li, *Ceram. Int.*, 2019, **45**, 11920–11926.
12. N. Thongyong, N. Chanlek, P. Srepusharawoot and P. Thongbai, *Molecules*, 2021, **26**, 6952.
13. N. Thongyong, W. Tuichai, N. Chanlek and P. Thongbai, *Ceram. Int.*, 2017, **43**, 15466–15471.
14. L. Yuan, L. Li, G. Li, D. Zhang, W. Han and D. Lu, *J. Alloys Compd.*, 2019, **780**, 8–16.
15. J. Liu, J. Xu, B. Cui, Q. Yu, S. Zhong, L. Zhang, S. Du and D. Xu, *J. Mater. Sci.: Mater. Electron.*, 2020, **31**, 5205–5213.
16. T. Nachaithong, P. Thongbai and S. Maensiri, *J. Eur. Ceram. Soc.*, 2017, **37**, 655–660.
17. G. Liu, H. Fan, J. Xu, Z. Liu and Y. Zhao, *RSC Adv.*, 2016, **6**, 48708–48714.
18. Z. Cao, J. Zhao, J. Fan, G. Li and H. Zhang, *Ceram. Int.*, 2021, **47**, 6711–6719.
19. C. Zhao and J. Wu, *ACS Appl. Mater. Interfaces*, 2018, **10**, 3680–3688.
20. W. Tuichai, S. Danwittayakul, N. Chanlek and P. Thongbai, *Mater. Res. Bull.*, 2019, **116**, 137–142.
21. Z. Li, J. Wu, D. Xiao, J. Zhu and W. Wu, *Acta Mater.*, 2016, **103**, 243–251.
22. W. Hu, K. Lau, Y. Liu, R. L. Withers, H. Chen, L. Fu, B. Gong and W. Hutchison, *Chem. Mater.*, 2015, **27**, 4934–4942.
23. X. Wei, W. Jie, Z. Yang, F. Zheng, H. Zeng, Y. Liu and J. Hao, *J. Mater. Chem. C*, 2015, **3**, 11005–11010.
24. N. Thongyong, N. Chanlek, P. Srepusharawoot, M. Takesada, D. P. Cann and P. Thongbai, *J. Eur. Ceram. Soc.*, 2022, **42**, 4944–4952.
25. N. Thanamoon, N. Chanlek, P. Srepusharawoot, P. Moontragoon and P. Thongbai, *J. Alloys Compd.*, 2023, **935**, 168095.

26 W. Dong, W. Hu, T. J. Frankcombe, D. Chen, C. Zhou, Z. Fu, L. Candido, G. Hai, H. Chen, Y. Li, R. L. Withers and Y. Liu, *J. Mater. Chem. A*, 2017, **5**, 5436–5441.

27 W. Dong, D. Chen, W. Hu, T. J. Frankcombe, H. Chen, C. Zhou, Z. Fu, X. Wei, Z. Xu, Z. Liu, Y. Li and Y. Liu, *Sci. Rep.*, 2017, **7**, 9950.

28 Y. Xue, Z. Wang, Y. Li, Z. Yi, X. Li and D. Wu, *J. Mater. Sci.: Mater. Electron.*, 2023, **34**, 864.

29 W. Dong, D. Chen, W. Hu, T. J. Frankcombe, H. Chen, C. Zhou, Z. Fu, X. Wei, Z. Xu, Z. Liu, Y. Li and Y. Liu, *Sci. Rep.*, 2017, **7**, 9950.

30 T. Nachaithong, P. Kidkhunthod, P. Thongbai and S. Maensiri, *J. Am. Ceram. Soc.*, 2017, **100**, 1452–1459.

31 Y. Q. Wu, X. Zhao, J. L. Zhang, W. B. Su and J. Liu, *Appl. Phys. Lett.*, 2015, **107**, 242904.

32 Y. Song, X. Wang, X. Zhang, Y. Sui, Y. Zhang, Z. Liu, Z. Lv, Y. Wang, P. Xu and B. Song, *J. Mater. Chem. C*, 2016, **4**, 6798–6805.

33 W. Tuichai, N. Thongyong, S. Danwittayakul, N. Chanlek, P. Srepusharawoot, P. Thongbai and S. Maensiri, *Mater. Des.*, 2017, **123**, 15–23.

34 C. Yang, M.-Y. Tse, X. Wei and J. Hao, *J. Mater. Chem. C*, 2017, **5**, 5170–5175.

35 R. D. Shannon, *Acta Crystallogr.*, 1976, **A32**, 751–767.

36 H. Zhao, F. Pan and Y. Li, *J. Materiomics*, 2017, **3**, 17–32.

37 G. Kresse and J. Furthmüller, *Comput. Mater. Sci.*, 1996, **6**, 15–50.

38 N. Sapawe, A. A. Jalil, S. Triwahyono, S. H. Adam, N. F. Jaafar and M. A. H. Satar, *Appl. Catal., B*, 2012, **125**, 311–323.

39 M. Zhu, H. Zhang, S. W. L. Favier, Y. Zhao, H. Guo and Z. Du, *J. Mater. Sci. Technol.*, 2022, **105**, 286–292.

40 H. Peng, P. Liang, X. Zhou, Z. Peng, Y. Xiang, X. Chao and Z. Yang, *J. Am. Ceram. Soc.*, 2019, **102**, 970–975.

41 W. Tuichai, S. Danwittayakul, N. Chanlek, M. Takesada, A. Pengpad, P. Srepusharawoot and P. Thongbai, *ACS Omega*, 2021, **6**, 1901–1910.

42 J. C. Parker and R. W. Siegel, *Appl. Phys. Lett.*, 1990, **57**, 943–945.

43 C. Yang, X. Wei and J. Hao, *Ceram. Int.*, 2018, **44**, 12395–12400.

44 M.-Y. Tse, X. Wei and J. Hao, *Phys. Chem. Chem. Phys.*, 2016, **18**, 24270–24277.

45 L. Zhenwei, L. Xuan, W. Wenjuan and W. Jiagang, *J. Am. Ceram. Soc.*, 2017, **100**, 3004–3012.

46 J. Boonlakhorn, N. Chanlek, J. Manyam, P. Srepusharawoot, S. Krongsuk and P. Thongbai, *J. Adv. Ceram.*, 2021, **10**, 1243–1255.

47 M. N. Rahaman and R. Manalert, *J. Eur. Ceram. Soc.*, 1998, **18**, 1063–1071.

48 J. Liu, L. Wang, X. Yin, Q. Yu and D. Xu, *Ceram. Int.*, 2020, **46**, 12059–12066.

49 W. Tuichai, S. Danwittayakul, N. Chanlek, P. Srepusharawoot, P. Thongbai and S. Maensiri, *RSC Adv.*, 2017, **7**, 95–105.

50 N. Thongyong, P. Srepusharawoot, W. Tuichai, N. Chanlek, V. Amornkitbamrung and P. Thongbai, *Ceram. Int.*, 2018, **44**, S145–S147.

51 X.-g. Zhao, P. Liu, Y.-C. Song, A.-p. Zhang, X.-m. Chen and J.-p. Zhou, *Phys. Chem. Chem. Phys.*, 2015, **17**, 24475.

52 C. H. Kim, Y. H. Jang, S. J. Seo, C. H. Song, J. Y. Son, Y. S. Yang and J. H. Cho, *Phys. Rev. B: Condens. Matter Mater. Phys.*, 2012, **85**, 245210.

53 J. Liu, C.-G. Duan, W.-G. Yin, W. Mei, R. Smith and J. Hardy, *Phys. Rev. B: Condens. Matter Mater. Phys.*, 2004, **70**, 144106.

54 J. Liu, Y. Sui, C.-g. Duan, W.-N. Mei, R. W. Smith and J. R. Hardy, *Chem. Mater.*, 2006, **18**, 3878–3882.

55 C. C. Wang and L. W. Zhang, *Appl. Phys. Lett.*, 2006, **88**, 042906.

56 L. Li, T. Lu, N. Zhang, J. Li and Z. Cai, *J. Mater. Chem. C*, 2018, **6**, 2283–2294.

57 T. Adams, D. Sinclair and A. West, *Phys. Rev. B: Condens. Matter Mater. Phys.*, 2006, **73**, 094124.